

# Observation of Strong Interlayer Coupling in MoS<sub>2</sub>/WS<sub>2</sub> Heterostructures

Jing Zhang, Jinhuan Wang, Peng Chen, Yue Sun, Shuang Wu, Zhiyan Jia, Xiaobo Lu, Hua Yu, Wei Chen, Jianqi Zhu, Guibai Xie, Rong Yang, Dongxia Shi,\* Xiulai Xu, Jianyong Xiang, Kaihui Liu, and Guangyu Zhang\*

Monolayer transition-metal dichalcogenides (TMDs) are 2D crystals beyond graphene with a direct bandgap varying from 0.8 to 2.1 eV.<sup>[1–8]</sup> Recently, great interest has been shown in using various TMDs as building blocks for van der Waals (vdW) heterostructures.<sup>[9–11]</sup> Such vdW heterostructures are not only fundamentally interesting but also technically important for novel semiconductor devices.<sup>[12–16]</sup> In general, the optical and electrical properties for such vertical hybrids could be strongly modulated by interlayer coupling, which could lead to an effective charge transfer and band structure recombination.<sup>[17]</sup> Theory has predicted that interlayer coupling evolves with twisted stacking angles in vdW heterostructures.<sup>[18]</sup> Vertical bilayers with commensurate crystallographic alignment (e.g., A–A or A–B stacked) have the shortest interlayer spacing thus the strongest interlayer coupling.<sup>[18]</sup> For misaligned vdW heterostructures fabricated by transfer process, it has been reported that the relatively weak interlayer coupling is attributed to repulsive steric effects of different interlayer separation.<sup>[19,20]</sup> Besides, interface contaminations, which are unavoidable in most transfer processes, are another source for degradation of the interface coupling. Recent progress has shown that such

problems could be potentially solved by in situ growth of one type of TMDs on another, a technique called vdW epitaxy.<sup>[21–26]</sup> However, in depth study on the interlayer coupling in the epitaxial grown bilayer TMD heterostructure is still absent and highly required.

In this paper, we report the epitaxial growth of MoS<sub>2</sub> on WS<sub>2</sub> to create bilayers of vdW heterostructures with clean interface and strong interlayer coupling via a two-step chemical vapor deposition (CVD) growth approach. The top-layer MoS<sub>2</sub> domains has dominated 0° and 60° lattice orientation relative to the bottom WS<sub>2</sub> layer, which are respectively of A–A and A–B stacking. We demonstrate that A–A and A–B stacked MoS<sub>2</sub>/WS<sub>2</sub> heterostructures show more efficient interlayer charge transfer and spatially separated exciton recombination than the transferred heterostructures due to the strong coupling in our sample. This strong interlayer coupling is evidenced by Raman layer breathing mode (LBM) and shear mode (SM), low temperature photoluminescence (PL) spectra, and electrical transport characterizations. Our results point up the possibility to design various TMDs heterostructures with controlled stacking for future photonic devices, solar cells, photodetectors, modulators, memory devices, and photocatalysis.

The MoS<sub>2</sub>/WS<sub>2</sub> bilayer heterostructures were grown via a two-step CVD process. **Figure 1a** illustrates the top and side atomistic structure views of vertically assembled MoS<sub>2</sub>/WS<sub>2</sub> on SiO<sub>2</sub>/Si substrates. Single-crystalline WS<sub>2</sub> sheets with domain size of 60–100 μm were firstly grown on 300 nm SiO<sub>2</sub>/Si substrates using sulfur (S) and tungsten trioxide (WO<sub>3</sub>) powder as precursors. Substrates were placed face down to the WO<sub>3</sub> precursor and the evaporation temperature of S and WO<sub>3</sub> is 120 °C and 900 °C, respectively, during the growth. Typical optical and AFM images of the as-grown WS<sub>2</sub> sheets are shown in **Figure 1b,d**, showing well-defined triangular shapes and atomic sharp edges. Using the as-grown WS<sub>2</sub> as a templet, we thus grew MoS<sub>2</sub> domains on top of WS<sub>2</sub> with S and MoO<sub>3</sub> as precursors (refer to Experimental Section for more growth details). As shown in **Figure 1c**, MoS<sub>2</sub> domains prefer to nucleate at the edges of bottom WS<sub>2</sub>; within the WS<sub>2</sub> domains, as-grown MoS<sub>2</sub> domains are also triangular and only have 0° and 60° orientation relative to the bottom WS<sub>2</sub> layer, suggesting a A–A and A–B stacking, respectively.<sup>[18]</sup> According to the previous reported work,<sup>[18]</sup> when  $\theta = 0^\circ$  and  $\theta = 60^\circ$ , there are three high-symmetry stacking configurations: the top layer S atoms are put above (1) the bottom W atoms (AA<sub>1</sub> and AB<sub>1</sub>), (2) the hexagonal centers (AA<sub>2</sub> and AB<sub>2</sub>), or (3) the bottom S atoms (AA<sub>3</sub> and AB<sub>3</sub>). For all configurations, AA<sub>1</sub> (AA) and AB<sub>1</sub> (AB) have the lowest energy and are the most stable configurations. TEM

Dr. J. Zhang, Dr. P. Chen, Dr. Y. Sun, Dr. S. Wu,  
Dr. X. B. Lu, Dr. H. Yu, Dr. W. Chen,  
Dr. J. Q. Zhu, Prof. R. Yang, Prof. D. X. Shi,  
Prof. X. L. Xu, Prof. G. Y. Zhang  
Beijing National Laboratory for Condensed  
Matter Physics and Institute of Physics  
Chinese Academy of Sciences  
Beijing 100190, China  
E-mail: dxshi@iphy.ac.cn; gy Zhang@iphy.ac.cn



J. H. Wang, Prof. K. H. Liu  
State Key Laboratory for Mesoscopic Physics  
School of Physics  
Peking University  
Beijing 100871, China

Dr. Z. Y. Jia, Prof. J. Y. Xiang  
State Key Laboratory for Metastable Materials Science and Technology  
Yanshan University  
Qinhuangdao 066004, China

Dr. G. B. Xie  
National Key Laboratory of Science and Technology on Space Microwave  
China Academy of Space Technology  
Xi'an 170100, China

Prof. K. H. Liu, Prof. G. Y. Zhang  
Collaborative Innovation Center of Quantum Matter  
Beijing 100190, China

DOI: 10.1002/adma.201504631

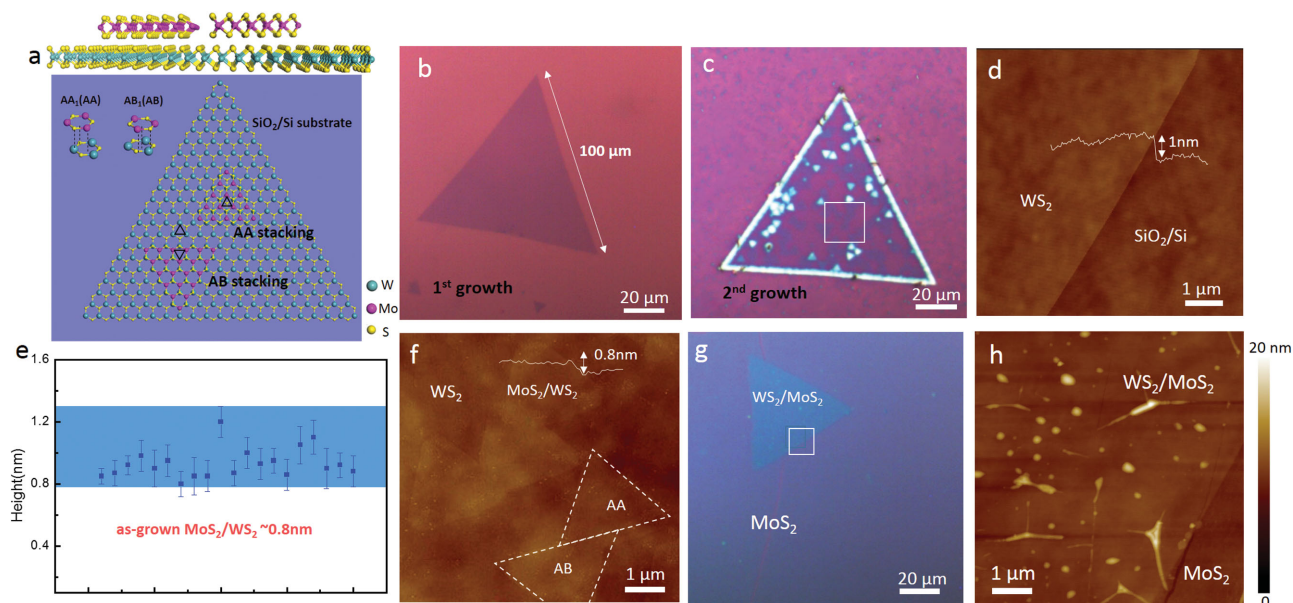


**Figure 1.** Characterization of as-grown and as-transferred vertically  $\text{MoS}_2/\text{WS}_2$  heterostructures. a) Top and side views for atomistic illustration of vertically assembled A–A and A–B stacked  $\text{MoS}_2/\text{WS}_2$  bilayers on  $\text{SiO}_2/\text{Si}$  substrate. b) Optical image of the first grown triangular  $\text{WS}_2$  domains on  $\text{SiO}_2/\text{Si}$ . c) Optical image of as-grown  $\text{MoS}_2$  triangular domains on the top of triangular  $\text{WS}_2$  domains. d) AFM image of the first grown  $\text{WS}_2$  domain with the monolayer thickness on  $\text{SiO}_2/\text{Si}$ . e) Statistic thickness distribution of as-grown monolayer  $\text{MoS}_2$  domains on  $\text{WS}_2$  layers. f) AFM image of atomically flat as-grown  $\text{MoS}_2$  on  $\text{WS}_2$  with A–A and A–B stacking. g, h) Optical and AFM images of as-transferred random stacking  $\text{MoS}_2/\text{WS}_2$  heterostructure with unintentional trapped bubbles and contaminations.

date of reported similar  $\text{MoS}_2/\text{WS}_2$  structure<sup>[25]</sup> can confirm the existence of AB ( $\text{AB}_1$ ) stacking bilayers ( $60^\circ$  orientation) consistent with atomic structure illustration in Figure 1a. Thus, the twist angle of vertically stacked bilayers can be determined by the relative orientation of the top and bottom triangular shape. We attributed the AA-stacking to  $\theta = 0^\circ$  and the AB-stacking to  $\theta = 60^\circ$  in Figure 1f. Figure 1f also shows an AFM image of triangular  $\text{MoS}_2$  domains on  $\text{WS}_2$  with sharp edges. The lateral size of these domains is about 2–3  $\mu\text{m}$  and the average height of  $\approx 0.8$  nm, corresponding to a monolayer thickness as illustrated in Figure 1e. In contrast, the height of  $\text{MoS}_2$  on  $\text{SiO}_2$  is  $\approx 1$  nm (refer to Figure S1, Supporting Information for more information). These domains can form continuous monolayer  $\text{MoS}_2$  film on  $\text{WS}_2$  by prolonged growth time. We also fabricated the  $\text{MoS}_2/\text{WS}_2$  vertical bilayers with random stacking orientation by transfer techniques as illustrated in Figure 1g, h. The top monolayer  $\text{MoS}_2$  layer for transfer is a polycrystalline continuous film grown on a sapphire substrate (more growth details of  $\text{MoS}_2$  monolayers shown in Figure S2, Supporting Information). As indicated by AFM images in Figure 1g, h, the interfacial morphology of epitaxial heterostructures is free of contamination and much cleaner and smoother than the transferred structures.

According to previous theoretical predictions,<sup>[18,27]</sup> the interlayer coupling of  $\text{MoS}_2/\text{WS}_2$  is strongest for A–A and A–B stacking configurations since the interlayer distance is the shortest among all configurations. Such strong interlayer coupling would lead to a substantial shift of the phonon vibration modes for individual  $\text{MoS}_2$  or  $\text{WS}_2$  layer and efficient charge transfer between the two atomic layers. In order to confirm such speculations, we carried out Raman and

photoluminescence (PL) characterizations with 532 nm excitation laser at 1 mW for both epitaxial and transferred  $\text{MoS}_2/\text{WS}_2$  vdW heterostructures.

As illustrated in Figure 2b, Raman-active in-plane/out-of-plane vibration for individual monolayer  $\text{WS}_2$  and  $\text{MoS}_2$  on  $\text{SiO}_2$  locates at  $353\text{ cm}^{-1}/416\text{ cm}^{-1}$  and  $384\text{ cm}^{-1}/404\text{ cm}^{-1}$ , respectively, which are consistent with previous studies.<sup>[28,29]</sup> Raman spectra of the transferred samples only show a superpose signature of these vibration modes. However, the out-of-plane  $\text{A}_{1g}$  modes of  $\text{MoS}_2$  and  $\text{WS}_2$  stiffen for 3–4  $\text{cm}^{-1}$  for epitaxial  $\text{MoS}_2/\text{WS}_2$  heterostructures, revealing a sustainable strong interlayer coupling. Note that the position of a phonon vibration is proportional to the real-time atomic force constant matrix.<sup>[30]</sup> The interaction term in this matrix can be described as “spring” connecting two sulfur layers as illustrated in Figure 2a. When stacking  $\text{MoS}_2$  on  $\text{WS}_2$ , vdW term is introduced and make the “spring” harder.<sup>[18]</sup> Thus,  $\text{A}_{1g}$  mode increases as a consequence. Therefore, we could use the shift of  $\text{A}_{1g}$  to probe vdW interaction strength and interfacial contact quality.

Owing to this strong interlayer coupling and controllable stacking configuration in epitaxial  $\text{MoS}_2/\text{WS}_2$  bilayers, we are also able to observe other intriguing and new phonon modes such as layer-breathing mode (LBM) and shear mode (SM), which are challenging to probe previously due to the uncontrollable interfacial environment. The LBM and SM are corresponding to rigid out-of-plane and in-plane vibrations with adjacent layers rigidly oscillate coherently perpendicular or relative to each other<sup>[31–33]</sup> (illustrated in Figure 2a). These phonon modes are also sensitive and significant for probing layer thickness, stacking order, surface adsorbates, and contact quality of hybridization of 2D materials.

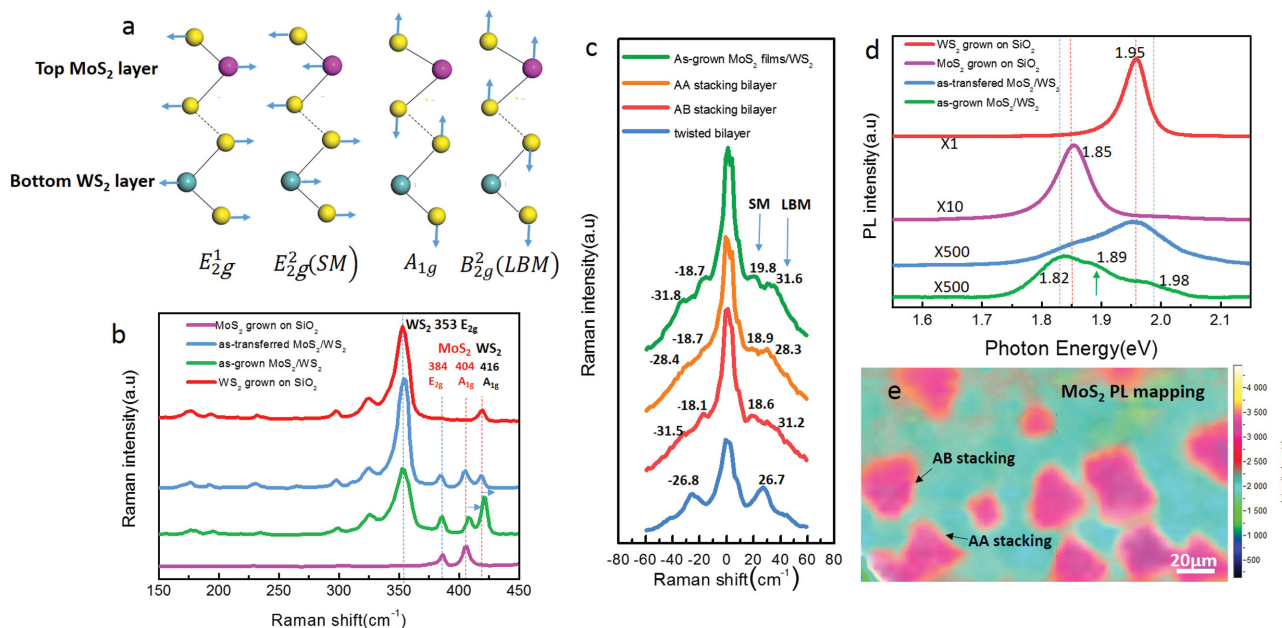


**Figure 2.** Raman and photoluminescence spectra of as-grown and as-transferred  $WS_2/MoS_2$  heterostructures. a) Schematic diagram of lattice structure and vibrational mode for bilayer heterostructure. b,d) Raman and PL spectra for as-grown, as-transferred  $MoS_2/WS_2$  heterostructures, and as-grown monolayer  $WS_2$  and  $MoS_2$ , respectively. c) Low-frequency Raman spectra of layer breathing mode (LBM) and shear mode (SM) for as-grown continuous  $MoS_2$  films on  $WS_2$ , A–A and A–B stacked, as-transferred twisted stacked  $MoS_2/WS_2$  heterostructures, respectively. e) PL intensity mapping for as-grown A–A and A–B stacking  $MoS_2/WS_2$ .

As shown in Figure 2c, prominent LBM peaks locate at 31.6, 28.3, 31.2, and 26.7  $cm^{-1}$  for as-grown continuous  $MoS_2$  films on the top of  $WS_2$ , A–A, A–B stacking and as-transferred twisted vdW heterostructures, respectively. Here, two prominent observations should be discussed in details. First, it is clearly observed that LBM frequency of A–B-stacked heterostructure increased by 2  $cm^{-1}$  compared with A–A-stacked bilayers, which can be attributed to slightly shorter interlayer distance and stronger interlayer coupling of A–B-stacked heterostructures. Second, it can be seen that the LBM vibrational frequency for as-transferred twisted  $MoS_2-WS_2$  decreased for 2–4  $cm^{-1}$  compared with as-grown A–B stacked ones, which indicates weak interlayer coupling and less packed efficiency for twisted bilayers. In this way, we can also demonstrate that our epitaxial vdW heterostructures provide stronger interlayer coupling and cleaner interface contact compared with artificially stacked heterostructures.

As reported previously, LBM can be observed in bilayer  $MoS_2$ ,  $WSe_2$ , or twisted stacked TMDs regardless of the stacking orientations.<sup>[31–34]</sup> However, this is not the case for SM vibrations; only when the two layers have perfect commensurate stacking are SM modes active since the lateral displacement can provide the restoring force. Since our epitaxial  $MoS_2/WS_2$  are A–A or A–B-stacked bilayers, the SM Raman peak can be clearly seen at  $\approx 18\text{ cm}^{-1}$  (Figure 2c). In this case, the rarely reported SM photon mode is strong evidence of our commensurate  $MoS_2/WS_2$  heterostructures with perfect crystallographic alignment, which provides an ideal platform to study unprecedented phonon structures and desirable phonon vibrational properties.

Figure 2d shows the room-temperature photoluminescence (PL) spectra of epitaxial and transferred  $MoS_2/WS_2$  heterostructures. Control samples of monolayer  $MoS_2$  and  $WS_2$  on  $SiO_2$

are also probed with strong A exciton emissions<sup>[35,36]</sup> locating at 1.95 and 1.85 eV, respectively. We can see that, for transferred vertically stacked heterostructures, each layer contributes independently to the overall signal. However, for epitaxial  $MoS_2/WS_2$  heterostructures, a slight PL position shift and an additional weak peak at 1.89 eV are observed, which can be attributed to the recombination of spatially separated carriers. Energy transfer and charge transfer are two main factors for PL quenching.<sup>[17]</sup> Note that PL intensity for both transferred twisted samples and CVD grown A–A and A–B stacked samples are strongly quenched (about 50 times weaker compared with monolayer  $MoS_2$ ). Energy transfer prefers to quench high energy exciton (1.95 eV) and enhance lower energy exciton (1.85 eV). As revealed in Figure 2d, the quenched PL for both  $WS_2$  and  $MoS_2$  exciton indicates that photoexcited charge transfer and spatially separated carrier recombination are the dominating processes in both the transferred and the epitaxial heterostructures.<sup>[17]</sup> Thus, intralayer optical recombination is largely suppressed in each of the  $MoS_2$  and  $WS_2$  individual layers. Note that the relative PL intensity of  $WS_2$  to  $MoS_2$  shows inverse signature for transferred and epitaxial samples. It can be attributed to the different defect densities in  $MoS_2$  and  $WS_2$  due to different growth and transfer process. Figure 2e shows a typical PL intensity mapping of A–A and A–B-stacked  $MoS_2/WS_2$  heterostructure regions. PL mapping can be used to confirm the spatial distribution of vertically stacked bilayers. There are no obvious PL intensity differences for  $0^\circ$  and  $60^\circ$  orientated  $MoS_2$  domains, suggesting that there are no dramatic variations in interlayer distance and coupling for both A–A and A–B stacking configurations.

To further study the interlayer exciton dynamics, we carried out PL measurements at liquid-nitrogen temperature (77 K) for

the epitaxial MoS<sub>2</sub>/WS<sub>2</sub> heterostructure. The results are shown in Figure 3a. Both WS<sub>2</sub> and MoS<sub>2</sub> exhibit an obvious upshift of PL peaks during cooling down. The A exciton emission position of MoS<sub>2</sub> shifts from 1.89 to 1.82 eV as plotted in Figure 3b, which can be attributed to the lattice expansion upon increased temperature.<sup>[22]</sup> Figure 3c presents the temperature-dependence of the full width at half maximum (FWHM) of MoS<sub>2</sub> PL, which varies from 76 meV at 300 K to 55 meV at 77 K. Usually, acoustic phonon scattering causes a linear increase of PL FWHM with temperature,<sup>[22]</sup> as demonstrated in this case. It was also noted that there is extra peak appearing at 1.98 eV at 77 K, which can be attributed to the recombination of interlayer carriers. The recombination efficiency is much weak at room temperature since this extra peak can rarely be seen at 300 K (see Figure 3a).

To understand the exciton recombination dynamics, we first discuss the band alignment of vertically stacked MoS<sub>2</sub>/WS<sub>2</sub> heterostructure as illustrated in Figure 3e. For the typical type-II heterostructure of MoS<sub>2</sub>/WS<sub>2</sub>, the maximum of the valence and the minimum of the conduction band are separated in WS<sub>2</sub> and MoS<sub>2</sub>, respectively. It was reported that the energy

gaps for MoS<sub>2</sub> and WS<sub>2</sub> are 2.39 eV and 2.31 eV, respectively. The energy difference between the maximum valence bands of MoS<sub>2</sub> and WS<sub>2</sub> is about 350 meV.<sup>[17,27]</sup> Photoexcited electrons and holes prefer to stay at separated layers. The excited electrons in WS<sub>2</sub> tend to accumulate in the conduction band of MoS<sub>2</sub> while holes generated in the valence band of the MoS<sub>2</sub> prefer to transfer to WS<sub>2</sub> at the interface. The interlayer radiative recombination of spatially separated carriers leads to the extra peaks locating at 1.94 eV mentioned above. Besides, the optical bandgap can be also obtained from the measured PL peaks. We may deduce the binding energy of the interlayer exciton to be 0.1 eV, which is much lower compared with monolayer MoS<sub>2</sub> (0.5 eV) and WS<sub>2</sub> (0.29 eV), which are consistent with reported results.<sup>[37]</sup>

Finally, we also performed electrical-transport measurements for the as-grown MoS<sub>2</sub>/WS<sub>2</sub> heterostructures on SiO<sub>2</sub>/Si substrate. Back-gated field-effect transistors based on single-crystalline MoS<sub>2</sub> domains on WS<sub>2</sub> were fabricated (Figure 4a). The device-fabrication process includes standard electron beam lithography (EBL), reactive ion etching (RIE) to remove unwanted MoS<sub>2</sub> layers, contact metal formation (10 nm Ti/40 nm Au)

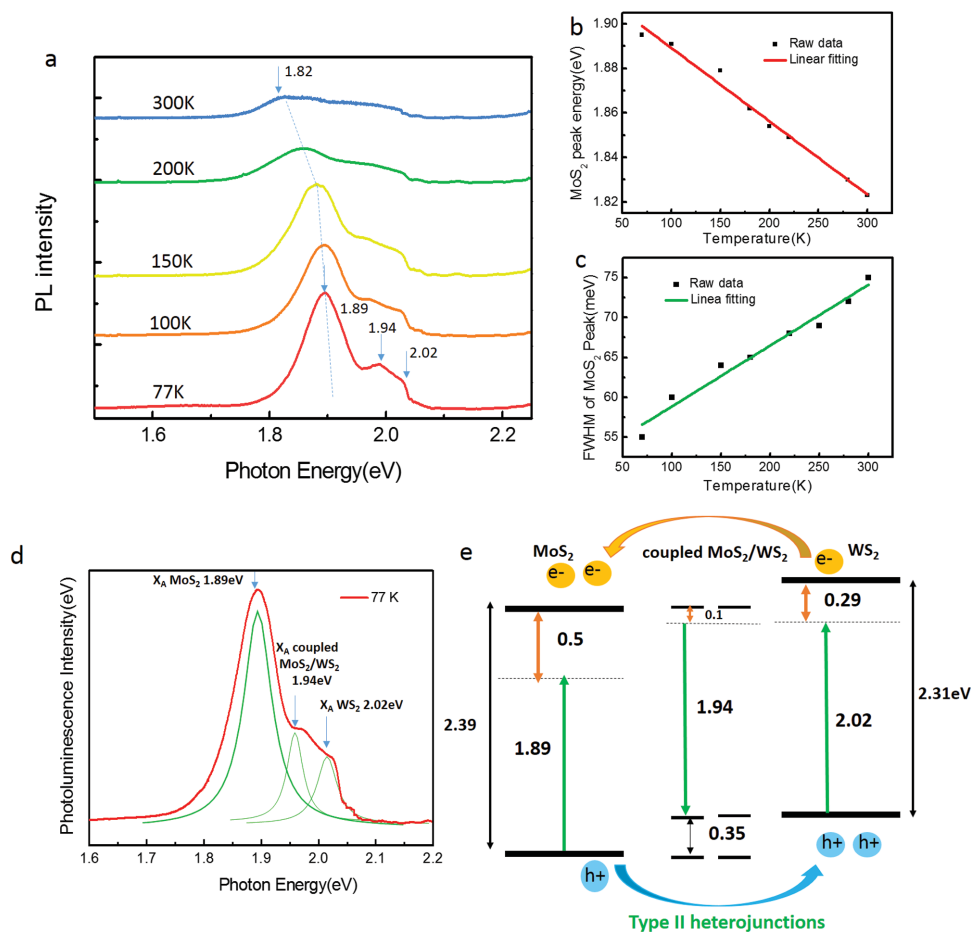


**Figure 3.** Low-temperature PL measurements of as-grown MoS<sub>2</sub>/WS<sub>2</sub> heterostructures and schematic diagram of band alignment. a) Temperature-dependence PL spectra from 300 to 77 K for as-grown samples. b,c) PL peak energy and FWHM for MoS<sub>2</sub> plotted as a function of temperature, respectively. d) PL spectra for as-grown heterostructure and the Lorentzian fitting at 77 K. e) The bandgap alignment of coupled MoS<sub>2</sub>/WS<sub>2</sub> heterostructure. The solid black, green, and orange double-arrow lines are the energy gap, optical gap, and exciton binding energy for the WS<sub>2</sub>, MoS<sub>2</sub>, and the coupled heterostructure, respectively.

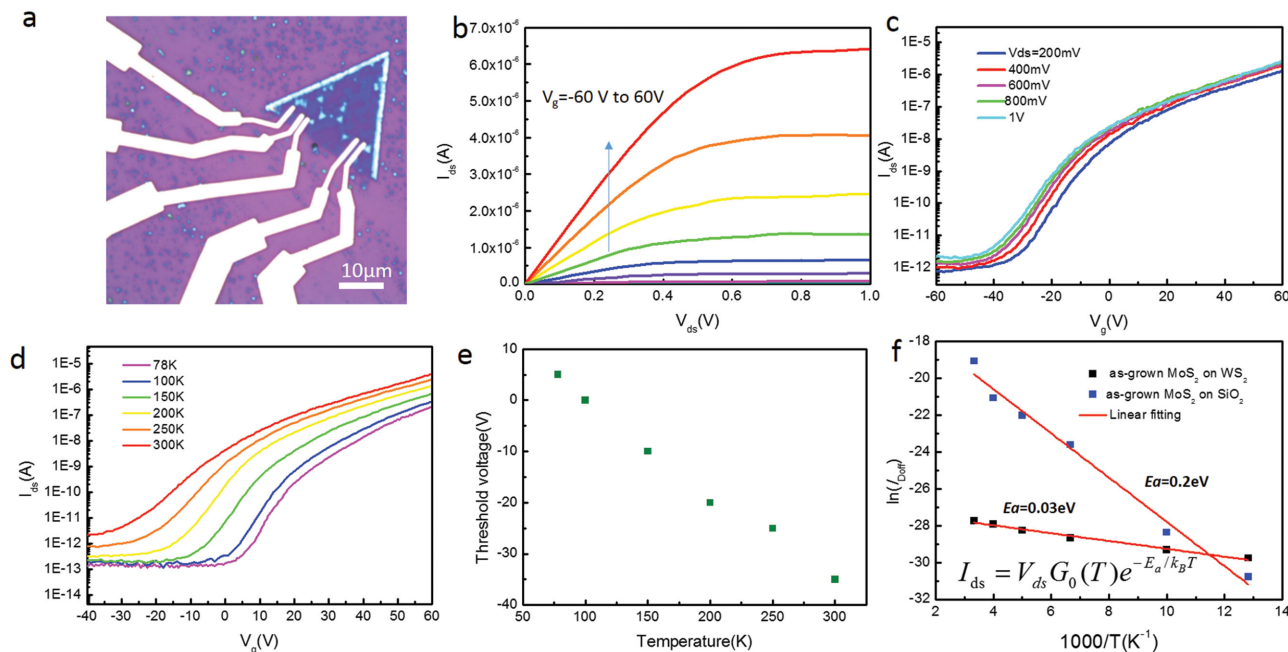


**Figure 4.** Electrical measurements of as-grown MoS<sub>2</sub>/WS<sub>2</sub> heterostructure. a) Optical image for MoS<sub>2</sub> field effect transistors on WS<sub>2</sub> substrate. b,c) Typical output and transfer curves for MoS<sub>2</sub> devices on WS<sub>2</sub>. d) Typical transfer curves for MoS<sub>2</sub> devices when decreasing temperature from 300 to 78 K. e) Threshold voltage plotted as a function of temperature. f) Temperature dependence of source drain current for MoS<sub>2</sub>/WS<sub>2</sub> and MoS<sub>2</sub>/SiO<sub>2</sub> systems plotted using thermally activated transport model.

by electron-beam deposition, and lift-off techniques. The devices were preannealed for 2 h at 400 °C in argon and hydrogen mixture to remove residual PMMA before electrical measurements in vacuum with a base pressure of  $<2 \times 10^{-7}$  mbar. Figure 4b,c are output and transfer curves of a typical device, revealing a typical n-type transistor behavior. A maximum on/off ratio over  $10^7$  at 300 K can be achieved and the threshold voltage is at  $-40$  V. We calculated the electron mobility of MoS<sub>2</sub> FET device using a standard transistor model and the resulting mobility was  $\approx 35$  cm<sup>2</sup> V<sup>-1</sup> s<sup>-1</sup>. We also performed cooling-down measurements on the same device (Figure 4d) and observed an obvious threshold voltage shift from  $-40$  V to 5 V when decreasing temperatures from 300 K to 78 K (Figure 4e). The position of threshold voltage reflects the doping level of device, which may come from: i) the intrinsic n doping caused by the sulfur vacancies; ii) the doping introduced by residuals; or iii) the doping from underneath WS<sub>2</sub>. Since (i) and (ii) should not change dramatically at varied temperatures, we attributed this shift of threshold voltage to process (iii); that is, the doping of MoS<sub>2</sub> by WS<sub>2</sub> comes from charge transfer between them. At a fixed gate voltage  $V_{bg} = 60$  V, the corresponding charge concentration at 300 K is  $n_{2D} = 7.2 \times 10^{12}$  cm<sup>-2</sup>, using parallel-plate capacitor model:  $n_{2D} = C_{ox} \Delta V_{bg} / e$ ; where  $C_{ox} = \epsilon_0 \epsilon_r / d_{ox}$ ,  $\epsilon_0 = 8.85 \times 10^{-12}$  F m<sup>-1</sup>,  $\epsilon_r = 3.9$ ,  $e = 1.6 \times 10^{-19}$  C,  $\Delta V_{bg} = V_{bg} - V_{bg,th1} = 100$  V. When decreasing the temperature from 300 to 78 K, charge transfer between the WS<sub>2</sub> and the MoS<sub>2</sub> makes a prominent contribution to the extra threshold voltage shift  $\Delta V_{th} = V_{th2} - V_{th1} = 45$  V, giving a typical p-doping concentration variation of  $\Delta n_{2d} = 3.24 \times 10^{12}$  cm<sup>-2</sup> in agreement with reported results.<sup>[17]</sup> Besides, we can also estimate the thermal activation energy  $E_a$  based on the thermally activated transport formula:<sup>[5]</sup>  $I_{ds} = V_{ds} G_0(T) \exp(-E_a / k_B T)$ ,

where  $I_{ds}$  is the source–drain current,  $V_{ds}$  is the source–drain voltage,  $G_0(T)$  is a temperature-dependent parameter, and  $k_B$  is the Boltzmann constant. As shown in Figure 4f, the calculated  $E_a$  is 0.03 eV. As a comparison,  $E_a$  is  $\approx 0.2$  eV for our MoS<sub>2</sub> on SiO<sub>2</sub>.<sup>[38]</sup> Note that  $E_a$  presents the Fermi level shifting modulated by doping between conduction and valence bands. This much smaller  $E_a$  for MoS<sub>2</sub> on WS<sub>2</sub> indicates that charge transfer between them is responsible for the temperature-dependent threshold voltage shifting.

In conclusion, we achieved epitaxial growth of MoS<sub>2</sub>/WS<sub>2</sub> bilayers with perfectly aligned A–A and A–B stacking configurations via a two-step CVD process. The strong interlayer coupling and efficient interlayer charge transfer were systematically studied in as-grown MoS<sub>2</sub>/WS<sub>2</sub>, as confirmed by both optical and electrical measurements. Our work provides fundamental understanding of interlayer coupling and offers a nondestructive and convenient way to probe the interface environment in vdW heterostructures, which are crucial factors to modulate devices performance. Overall, it paves the way toward mass production of vdW heterostructures for future optoelectronic devices.

## Experimental Section

**Growth of MoS<sub>2</sub>/WS<sub>2</sub> Heterostructures:** The WS<sub>2</sub> triangular domains were first grown on SiO<sub>2</sub> (300 nm)/p++Si substrates by pre-cleaned with acetone and isopropyl alcohol, followed by treated in Piranha solution (H<sub>2</sub>SO<sub>4</sub>:H<sub>2</sub>O<sub>2</sub>  $\approx$  3:1) for 2 h. The growth process was carried out in three-zone CVD system with 1 in. quartz tube using WO<sub>3</sub> (99.999%; Alfa Aesar), MoO<sub>3</sub> (99.999%; Alfa Aesar) and S (99.99%; Alfa Aesar) powder as the precursor. Each of the three temperature zones was heated to preset values at a rate of 25 °C min<sup>-1</sup>, respectively. Sulfur and MoO<sub>3</sub> sources

were separately loaded in two mini-quartz tubes (diameter  $\approx$  10 mm) in our design, which provides a stable evaporation of sulfur and MoO<sub>3</sub> sources by avoiding any cross-contaminations during the growth. Each temperature zone was kept stable for 20 min prior to growth. The precursor powders were preplaced outside of the furnace and rapidly loaded from outside into each zone for starting the growth. During the growth, Argon was used as carrying gas at a flow rate of 130 sccm and the vacuum pressure was kept at 0.7 Torr. Note that our heterostructure growth follows a two-step process, the WS<sub>2</sub> domains were firstly grown on SiO<sub>2</sub> substrates followed by second growth of MoS<sub>2</sub> on top of WS<sub>2</sub>. The typical temperature for each three zones is 115 °C, 560 °C, 800 °C, respectively, for MoS<sub>2</sub> growth.

**Fabrication of As-Transferred Twisted WS<sub>2</sub>/MoS<sub>2</sub> Heterostructure:** The continuous monolayer MoS<sub>2</sub> films were firstly grown on sapphire substrates. Then MoS<sub>2</sub>/sapphire substrates were first spin-coated by PMMA (950 5% in anisole) at 3000 rpm for 60 s and baked at 180 °C for 1 min and repeat that process again. Then PMMA-coated samples were soaked in KOH solution (1 M) to etch away Al<sub>2</sub>O<sub>3</sub> to separate the PMMA/MoS<sub>2</sub> layer from sapphire. The floated layer was cleaned by DI water and then transferred onto WS<sub>2</sub>/SiO<sub>2</sub> substrate. Acetone was used to dissolve the PMMA for 10 h at room temperature.

**Fabrication of the MoS<sub>2</sub>/WS<sub>2</sub> FET Devices:** 5% 495 PMMA in anisole was spin-coated at 4000 rpm on the as-prepared samples, and then continuous MoS<sub>2</sub> films on SiO<sub>2</sub>/Si substrates and thick MoS<sub>2</sub> layers on WS<sub>2</sub> edges were etched away using a Raith e-beam lithography system and oxygen plasma-active ion etching system (PlasmaLab 80 Plus, Oxford Instruments Company). The plasma power, oxygen pressure, flow rate, and etching time were 50 W, 0.1 Torr, 100 sccm, and 8 s, respectively. Metal electrodes were then made for the patterned MoS<sub>2</sub> by metal-film deposition and lift-off techniques. The as-fabricated devices were annealed before electrical measurements were performed with Agilent semiconductor parameter analyzer (4156 C) under high vacuum in a four-probe station system.

**Characterizations of As-Grown MoS<sub>2</sub>/WS<sub>2</sub> Heterostructure:** Ordinary Raman spectroscopy was carried out using a Horiba Jobin Yvon LabRAM HR-Evolution Raman microscope. The low-frequency Raman spectroscopy was carried out with our home-built setup-based Bragg gratings. The excitation light is a 532 nm laser, with an estimated laser spot size of 1  $\mu$ m and the laser power of 1 mW. High-resolution photoluminescence mapping images were obtained with 50 $\times$  objective, 600 grooves/mm grating, and 500 nm mapping step. The surface morphology images of MoS<sub>2</sub>/WS<sub>2</sub> heterostructures were characterized by atomic force microscope (AFM) (MultiMode IIIA, Veeco Instruments Inc.) using tapping mode at ambient atmosphere.

## Supporting Information

Supporting Information is available from the Wiley Online Library or from the author.

## Acknowledgements

This work was supported by the National Natural Science Foundation of China (NSFC) under the grant Nos. 61325021, 51572289, 91323304, the National Basic Research Program of China (973 Program) under the grant Nos. 2013CB934500 and 2013CBA01602, and Strategic Priority Research Program (B) of the Chinese Academy of Sciences (Grant No. XDB07010100). K.L. acknowledges supports from National Science Foundation of China (11474006, 91433102, 51522201) and National Program for Thousand Young Talents of China. X.X. thanks the financial support from the Hundred Talents Program of Chinese Academy of Sciences.

Received: September 20, 2015

Revised: November 3, 2015

Published online: December 28, 2015

- [1] K. F. Mak, C. Lee, J. Hone, J. Shan, T. F. Heinz, *Phys. Rev. Lett.* **2010**, *105*, 136805.
- [2] Q. H. Wang, K. Kalantar-Zadeh, A. Kis, J. N. Coleman, M. S. Strano, *Nat. Nanotechnol.* **2012**, *7*, 699.
- [3] B. Radisavljevic, A. Radenovic, J. Brivio, V. Giacometti, A. Kis, *Nat. Nanotechnol.* **2011**, *6*, 147.
- [4] B. W. Baugher, H. O. Churchill, Y. Yang, P. Jarillo-Herrero, *Nano Lett.* **2013**, *13*, 4212.
- [5] B. Radisavljevic, A. Kis, *Nat. Mater.* **2013**, *12*, 815.
- [6] S. Ghatak, A. N. Pal, A. Ghosh, *ACS Nano* **2011**, *5*, 7707.
- [7] Z. Yin, H. Li, H. Li, L. Jiang, Y. Shi, Y. Sun, G. Lu, Q. Zhang, X. Chen, H. Zhang, *ACS Nano* **2012**, *6*, 74.
- [8] W. J. Zhang, J. K. Huang, C. H. Chen, Y. H. Chang, Y. J. Cheng, L. J. Li, *Adv. Mater.* **2013**, *25*, 3456.
- [9] A. K. Geim, I. V. Grigorieva, *Nature* **2013**, *499*, 419.
- [10] X. Wang, F. Xia, *Nat. Mater.* **2015**, *14*, 264.
- [11] P. Chen, J. Y. Xiang, H. Yu, J. Zhang, G. B. Xie, R. Yang, D. X. Shi, G. Y. Zhang, *2D Mater.* **2015**, *2*, 034009.
- [12] M. Sup Choi, G. H. Lee, Y. J. Yu, D. Y. Lee, S. Hwan Lee, P. Kim, J. Hone, W. Jong Yoo, *Nat. Commun.* **2013**, *4*, 1624.
- [13] J. Pu, Y. Yomogida, K. K. Liu, L. J. Li, Y. Iwasa, T. Takenobu, *Nano Lett.* **2012**, *12*, 4013.
- [14] F. Withers, O. Del Pozo-Zamudio, A. Mishchenko, A. P. Rooney, A. Gholinia, K. Watanabe, T. Taniguchi, S. J. Haigh, A. K. Geim, A. I. Tartakovskii, K. S. Novoselov, *Nat. Mater.* **2015**, *14*, 301.
- [15] W. J. Yu, Y. Liu, H. Zhou, A. Yin, Z. Li, Y. Huang, X. Duan, *Nat. Nanotechnol.* **2013**, *8*, 952.
- [16] W. Zhang, C. P. Chuu, J. K. Huang, C. H. Chen, M. L. Tsai, Y. H. Chang, C. T. Liang, Y. Z. Chen, Y. L. Chueh, J. H. He, M. Y. Chou, L. J. Li, *Sci. Rep.* **2014**, *4*, 3826.
- [17] X. Hong, J. Kim, S. F. Shi, Y. Zhang, C. Jin, Y. Sun, S. Tongay, J. Wu, Y. Zhang, F. Wang, *Nat. Nanotechnol.* **2014**, *9*, 682.
- [18] K. Liu, L. Zhang, T. Cao, C. Jin, D. Qiu, Q. Zhou, A. Zettl, P. Yang, S. G. Louie, F. Wang, *Nat. Commun.* **2015**, *5*, 4966.
- [19] S. Tongay, W. Fan, J. Kang, J. Park, U. Koldemir, J. Suh, D. S. Narang, K. Liu, J. Ji, J. Li, R. Sinclair, J. Wu, *Nano Lett.* **2014**, *14*, 3185.
- [20] H. Fang, C. Battaglia, C. Carraro, S. Nemsak, B. Ozdol, J. S. Kang, H. A. Bechtel, S. B. Desai, F. Kronast, C. S. Fadley, E. Yablonovitch, R. Maboudian, A. Javey, *Proc. Natl. Acad. Sci. USA* **2014**, *111*, 6198.
- [21] W. Yang, G. Chen, Z. Shi, C. C. Liu, L. Zhang, G. Xie, M. Cheng, D. Wang, R. Yang, D. Shi, K. Watanabe, T. Taniguchi, Y. Yao, Y. Zhang, G. Zhang, *Nat. Mater.* **2013**, *12*, 792.
- [22] Y. Kobayashi, S. Sasaki, S. Mori, H. Hibino, Z. Liu, K. Watanabe, T. Taniguchi, K. Suenaga, Y. Maniwa, Y. Miyata, *ACS Nano* **2015**, *9*, 4056.
- [23] Y. Yu, S. Hu, L. Su, L. Huang, Y. Liu, Z. Jin, A. A. Puzosky, D. B. Geohegan, K. W. Kim, Y. Zhang, L. Cao, *Nano Lett.* **2015**, *15*, 486.
- [24] Y. Shi, W. Zhou, A. Y. Lu, W. Fang, Y. H. Lee, A. L. Hsu, S. M. Kim, K. K. Kim, H. Y. Yang, L. J. Li, J. C. Idrobo, J. Kong, *Nano Lett.* **2012**, *12*, 2784.
- [25] Y. Gong, J. Lin, X. Wang, G. Shi, S. Lei, Z. Lin, X. Zou, G. Ye, R. Vajtai, B. I. Yakobson, H. Terrones, M. Terrones, Beng. K. Tay, J. Lou, S. T. Pantelides, Z. Liu, W. Zhou, P. M. Ajayan, *Nat. Mater.* **2014**, *13*, 1135.
- [26] H. Heo, J. H. Sung, G. Jin, J. H. Ahn, K. Kim, M. J. Lee, M. H. Jo, *Adv. Mater.* **2015**, *27*, 3803.
- [27] K. Košmider, J. Fernández-Rossier, *Phys. Rev. B* **2013**, *87*, 075451.
- [28] A. Berkdemir, H. R. Gutierrez, A. R. Botello-Mendez, N. Perea-Lopez, A. L. Elias, C.-I. Chia, B. Wang, V. H. Crespi, F. Lopez-Urias, J.-C. Charlier, H. Terrones, M. Terrones, *Sci. Rep.* **2013**, *3*, 1755.
- [29] C. Lee, H. Yan, L. E. Brus, T. F. Heinz, J. Hone, S. Ryu, *ACS Nano* **2010**, *4*, 2695.
- [30] K. G. Zhou, F. Withers, Y. Cao, S. Hu, G. Yu, C. Casiraghi, *ACS Nano* **2014**, *8*, 9914.
- [31] X. Zhang, W. P. Han, J. B. Wu, S. Milana, Y. Lu, Q. Q. Li, A. C. Ferrari, P. H. Tan, *Phys. Rev. B* **2013**, *87*, 115413.

- [32] A. A. Poretzky, L. Liang, X. Li, K. Xiao, K. Wang, M. Mahjouri-Samani, L. Basile, J. C. Idrobo, B. G. Sumpter, V. Meunier, D. B. Geohegan, *ACS Nano* **2015**, *9*, 6333.
- [33] Y. Zhao, X. Luo, H. Li, J. Zhang, P. T. Araujo, C. K. Gan, J. Wu, H. Zhang, S. Y. Quek, M. S. Dresselhaus, Q. Xiong, *Nano Lett.* **2013**, *13*, 1007.
- [34] C. H. Lui, Z. Ye, C. Ji, K.-C. Chiu, C.-T. Chou, T. I. Andersen, C. Means-Shively, H. Anderson, J.-M. Wu, T. Kidd, Y.-H. Lee, R. He, *Phys. Rev. B* **2015**, *91*, 165403.
- [35] G. Eda, H. Yamaguchi, D. Voiry, T. Fujita, M. Chen, M. Chhowalla, *Nano Lett.* **2011**, *11*, 5111.
- [36] A. Splendiani, L. Sun, Y. B. Zhang, T. S. Li, J. Kim, C. Y. Chim, G. Galli, F. Wang, *Nano Lett.* **2010**, *10*, 1271.
- [37] K. F. Mak, K. He, C. Lee, G. H. Lee, J. Hone, T. F. Heinz, J. Shan, *Nat. Mater.* **2013**, *12*, 207.
- [38] J. Zhang, H. Yu, W. Chen, X. Z. Tian, D. H. Liu, M. Cheng, G. B. Xie, W. Yang, R. Yang, D. X. Shi, G. Y. Zhang, *ACS Nano* **2014**, *8*, 6024.
-